Pseudo-acoustic vertical transverse isotropic migration velocity analysis using two-way wavefield propagation

Carlo Fortini

ABSTRACT

Wave-Equation Migration Velocity Analysis (WEMVA) is widely used as a tool to reconstruct a model of the subsurface, such that some features of the migrated image are met. I show an anisotropic WEMVA workflow based on the Vertical Transverse Isotropic (VTI) approximation for the velocity model and a pseudo-acoustic anisotropic two-way wave-equation modeling engine. I derive the theory of WEMVA starting from the gradients of the anisotropic Full Waveform Inversion (FWI) that provides the input images for the velocity analysis. In doing so, I introduce the concept of *generalized images* that defines the FWI gradients computed with respect to the anisotropic parameters as different images of the subsurface. The results of some preliminary tests on the use of the generalized images as input for WEMVA suggest that this approach could help improving the accuracy and rate of convergence of WEMVA.

INTRODUCTION

Velocity model building is a key element in the context of seismic processing and is still one of the most challenging problems in the exploration industry. Currently, velocity building is conducted with techniques that work either in the *data-space* or *image-space*. To the first class belong all those algorithms that go under the name of Full Waveform Inversion (FWI); whereas, to the second class belong the so-called Wave Equation Migration Velocity Analysis (WEMVA) processes. There are various advantages that drive to the use of image-space techniques as opposed to data-space techniques: First, the migrated images are usually cleaner than recorded data. Moreover, the requirements for the initial model are less strict for WEMVA rather than FWI techniques.

Most of the time, WEMVA is conducted under an isotropic approximation of the subsurface model, neglecting its anisotropic characteristics. However, the increasing offset and azimuth in recent seismic data acquisition has heightened the need for an anisotropic parametrization of the velocity model. Neglecting the anisotropy can, in fact, lead to a wrong interpretation of the subsurface structures. In many cases, a Vertical Transverse Isotropic (VTI) approximation can be used to more accurately

describe the subsurface. Li and Biondi (2011) showed that WEMVA can be successfully used to retrieve an anisotropic model using a one-way VTI wave-equation as propagation engine. Many authors (Duveneck et al. (2008); Fletcher et al. (2009); Zhang and Zhang (2009)) proposed migration and modeling algorithms schemes for VTI media, primarily based on the *pseudo-acoustic* approximation first proposed by Alkhalifah (1998). Because the anisotropic parameters are sensitive to events that propagate with large angles, the use of two-way wave-equation modeling algorithm can provide significant improvement to the results of anisotropic WEMVA (Li et al., 2012).

In this paper, I show an anisotropic WEMVA workflow based on two-way wave-equation propagation engine. I first introduce briefly the wave-equation I use; and then, I derive the computation of the WEMVA gradients. In doing so, I start from the gradients of FWI that provide the input image for WEMVA. I also show some preliminary results on the use of the anisotropic generalized images as input for the image-space velocity model inversion.

ACOUSTIC VERTICAL TRANSVERSE ISOTROPIC WAVE-FIELD MODELING

To avoid complications coming from the presence of *shear waves* and for computational efficiency, wave propagation modeling with two-way wave-equation is usually conducted under the *pseudo-acoustic* VTI approximation (Alkhalifah, 1998). This approximation consists of setting the shear-wave velocity to zero in the exact elastic wave equations and leads to the following system of partial differential equations (Duveneck et al., 2008):

$$\begin{cases} \dfrac{1}{v_p^2}\dfrac{\partial^2 p_h}{\partial t^2} = (1+2\varepsilon)\dfrac{\partial^2 p_h}{\partial x^2} + \sqrt{1+2\delta}\dfrac{\partial^2 p_v}{\partial z^2} + f_h \\ \dfrac{1}{v_p^2}\dfrac{\partial^2 p_v}{\partial t^2} = \sqrt{1+2\delta}\dfrac{\partial^2 p_h}{\partial x^2} + \dfrac{\partial^2 p_v}{\partial z^2} + f_v, \end{cases} \tag{1}$$

where $\epsilon(x,y,z)$, $\delta(x,y,z)$ and $v_p(x,y,z)$ are, respectively, the anisotropic Thomsen parameters (Thomsen, 1986) and the vertical P-wave velocity. $p_h(x,y,z,t)$ and $p_v(x,y,z,t)$ are the horizontal and vertical normal stresses. Similarly, $f_h(x,y,z,t)$ and $f_v(x,y,z,t)$ are the horizontal and vertical source terms. The system 1 can be re-written in a matrix-vector notation as follows:

$$\mathbf{L}(v_p,\varepsilon,\delta)\mathbf{p} = \mathbf{f}, \tag{2}$$

where $\mathbf{p} = [p_h, p_v]^T$, $\mathbf{f} = [f_h, f_v]^T$ is the source term and

$$\mathbf{L}(v_p, \varepsilon, \delta) = \begin{bmatrix} \frac{1}{v_p^2}\frac{\partial^2}{\partial t^2} - (1+2\varepsilon)\frac{\partial^2}{\partial x^2} & -\sqrt{1+2\delta}\frac{\partial^2}{\partial z^2} \\ -\sqrt{1+2\delta}\frac{\partial^2}{\partial x^2} & \frac{1}{v_p^2}\frac{\partial^2}{\partial t^2} - \frac{\partial^2}{\partial z^2} \end{bmatrix}. \tag{3}$$

When both ϵ and δ are set to zero, system 1 is equivalent to the isotropic acoustic second-order wave-equation.
Because the equations previously presented have been derived with the acoustic VTI approximation, they are kinematically equivalent to acoustic VTI equations previously described in the literature (e.g., Fletcher et al. (2009); Zhang and Zhang (2009)) and share both the benefits and drawbacks of all the equations based on an acoustic approximation. They have the well-known problem of source-generated shear waves (Grechka et al., 2004), which for the purposes of P-wave modeling are regarded as artifacts. In my work, I always consider the case of an acquisition surface placed in an isotropic layer; and thus, the source-generated shear waves does not constitute a problem. Another consequence of the acoustic VTI approximation is the condition $\epsilon \geq \delta$ to ensure stability.

The system of equation in 1 is a special case of the one presented in Li et al. (2012) for the specific case of a constant density medium. I used these equations as the basis for an anisotropic two-way modeling and reverse-time migration implementation for all the examples in this paper.

IMAGING PRINCIPLE FOR VERTICAL TRANSVERSE ISOTROPIC MIGRATION

What is usually referred to as the subsurface image in the context of seismic migration can be computed as the first gradient of a Full Waveform Inversion (FWI) inverse problem (Tarantola, 1984), when the initial model does not contain any sharp contrasts. The objective function that is usually minimized for solving the FWI problem is defined in the *data-space* as follows:

$$J_{\text{FWI}} = \frac{1}{2}\left\langle d_{\text{obs}} - d_{\text{est}}, d_{\text{obs}} - d_{\text{est}} \right\rangle, \tag{4}$$

where d_{obs} is the recorded data and d_{est} is the data estimated using the wave-equation in 1 and the current models (ϵ, δ, v_p). d_{est} is simply obtained by the sampling of the wavefield $\mathbf{p}$ at the location of the original acquisition surface where d was recorded. At the very first iteration, we usually have only a smooth estimate for the subsurface models. If we only account for the reflection events (neglecting the diving waves, the refractions and the direct arrivals), then $d_{\text{est}} = 0$ because no reflection events can be generated when using a smooth model. The FWI gradient would try to introduce exactly those interfaces needed to explain the reflection events recorded and observed in the data giving as output what we usually call "migrated image."

Li et al. (2012) show that the gradient of the FWI objective function can be computed using the *adjoint-state method*. The final result is the following:

$$\nabla_{\mathbf{m}} J_{\text{FWI}} = -\left\langle \mathbf{q}, \frac{\partial \mathbf{L}}{\partial \mathbf{m}} \mathbf{p} \right\rangle, \tag{5}$$

where $\langle , \rangle$ indicates the scalar product in time and $\mathbf{q} = [q_h(x,y,z,t), q_v(x,y,z,t)]$ is the wavefield computed by back-propagating the data residual $d_{\text{obs}} - d_{\text{est}}$. $\mathbf{m}$ indicates the vector of the model parameters that describe the subsurface. Depending on the case under analysis, $\mathbf{m}$ can be either 1D or multidimensional. For the isotropic case, $\mathbf{m} = [v_p]$; while for the anisotropic scenario described in the previous section, $\mathbf{m}$ is the vector of the three components of the anisotropic subsurface model ($\mathbf{m} = [v_p, \epsilon, \delta]^T$). Equation 5 can be expanded as

$$\begin{aligned}
\nabla_{v_p} J_{\text{FWI}} &= -\left\langle \mathbf{q}, \frac{\partial \mathbf{L}}{\partial v_p} \mathbf{p} \right\rangle; \\
\nabla_{\varepsilon} J_{\text{FWI}} &= -\left\langle \mathbf{q}, \frac{\partial \mathbf{L}}{\partial \varepsilon} \mathbf{p} \right\rangle; \\
\nabla_{\delta} J_{\text{FWI}} &= -\left\langle \mathbf{q}, \frac{\partial \mathbf{L}}{\partial \delta} \mathbf{p} \right\rangle,
\end{aligned} \tag{6}$$

where

$$\frac{\partial \mathbf{L}}{\partial v_p} = \begin{bmatrix} -\frac{2}{v_p^3}\frac{\partial^2}{\partial t^2} & 0 \\ 0 & -\frac{2}{v_p^3}\frac{\partial^2}{\partial t^2} \end{bmatrix}; \tag{7}$$

$$\frac{\partial \mathbf{L}}{\partial \epsilon} = \begin{bmatrix} -2\frac{\partial^2}{\partial x^2} & 0 \\ 0 & 0 \end{bmatrix}; \tag{8}$$

$$\frac{\partial \mathbf{L}}{\partial \delta} = \begin{bmatrix} 0 & -\frac{1}{\sqrt{1+2\delta}}\frac{\partial^2}{\partial z^2} \\ -\frac{1}{\sqrt{1+2\delta}}\frac{\partial^2}{\partial x^2} & 0 \end{bmatrix}. \tag{9}$$

The explicit expressions for the computation of the three gradients are

$$\begin{aligned}
\nabla_{v_p} J_{\text{FWI}} &= I_{v_p} = \frac{2}{v_p^3}\left(\int \frac{\partial^2 p_h}{\partial t^2} q_h dt + \int \frac{\partial^2 p_v}{\partial t^2} q_v dt \right); \\
\nabla_{\varepsilon} J_{\text{FWI}} &= I_{\epsilon} = 2\int \frac{\partial^2 p_h}{\partial x^2} q_h dt; \\
\nabla_{\delta} J_{\text{FWI}} &= I_{\delta} = \frac{1}{\sqrt{1+2\delta}}\left(\int \frac{\partial^2 p_h}{\partial x^2} q_h dt + \int \frac{\partial^2 p_v}{\partial z^2} q_v dt \right).
\end{aligned} \tag{10}$$

In analogy with the isotropic acoustic case in which the first FWI gradient is referred as "the image", I refer to the three components of the gradient of the VTI

FWI objective function (I_{v_p}, I_ϵ and I_δ) as *generalized images*. In fact, the expressions in equation 10 can be seen as generalized imaging principles for the VTI migration. From a kinematic point of view, they all contain the same events: They all give an image of the same subsurface interfaces. However, they are not equivalent in term of amplitudes and illumination of the subsurface reflectors. Figure 1 shows two angle gathers extracted from, respectively, I_{v_p} and I_ϵ for a simple synthetic example. The models used to both generate and compute the FWI gradients are all constant (v_p, ϵ and δ) with a single, sharp discontinuity that simulates a flat reflector positioned at $z = 1,800$ m.

The main difference between the two images is the lack of illumination at zero-incidence angle for the case of I_ϵ. This behavior is in accordance with the theory: Events traveling almost vertically have no sensitivity to the anisotropy parameter ϵ.

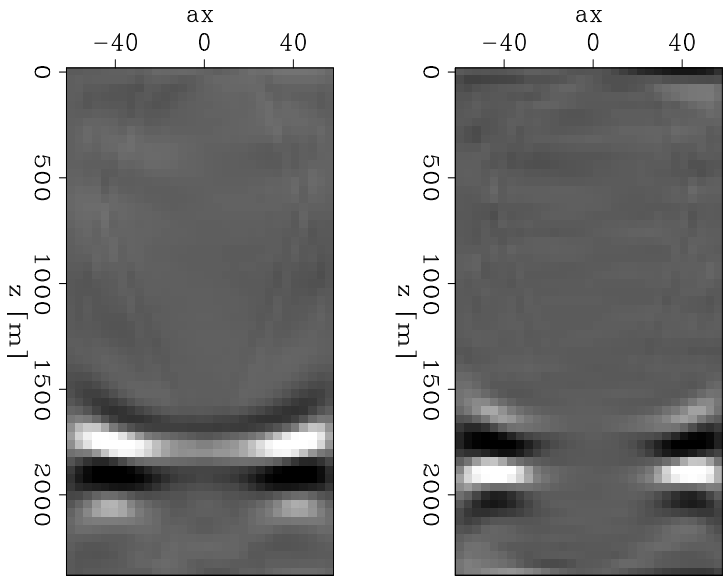

(a) (b)

Figure 1: Angle gathers extracted from (a) I_{v_p} and (b) I_ϵ. Notice the differences in the illumination. [**NR**]

ANISOTROPIC WAVE EQUATION MIGRATION VELOCITY ANALYSIS

Wave Equation Migration Velocity Analysis (WEMVA) is a nonlinear inversion process that aims at estimating a background (anisotropic) velocity model, such that a pre-selected objective function is minimized. Unlike FWI, the objective function for WEMVA is defined in the *image-space*. The generic objective function for WEMVA is

$$J_{\text{WEMVA}} = \frac{1}{2} \langle PI, PI \rangle \,, \tag{11}$$

where I is a seismic image and P is a *penalty* operator. P is usually chosen, such that the minimization of the objective function leads to a seismic image with some desired features. The most commonly used objective functions are

$$\begin{aligned} J_{\text{DSO}} &= \frac{1}{2} \langle \mathbf{h} I(\mathbf{x}, \mathbf{h}), \mathbf{h} I(\mathbf{x}, \mathbf{h}) \rangle \,; \\ J_{\text{PSM}} &= \frac{1}{2} \langle I(\mathbf{x}, \mathbf{h} = 0), I(\mathbf{x}, \mathbf{h} = 0) \rangle \,. \end{aligned} \tag{12}$$

I is expressed as a function of the position $\mathbf{x} = (x, y, z)$ and the subsurface offset shift (lag) $\mathbf{h} = [h_x, h_y]$ (Sava and Fomel, 2006). The former is the so-called *Differential Semblance Optimization* (DSO), while the latter is the *Power of Stack Migration* (PSM) (Symes and Kern (1994); Toldi (1989); Shen (2004)). The images used as input for WEMVA can be computed as shown in the previous section, solving the first step of the FWI. In particular, the image as a function of the Subsurface Offset Domain Common Image Gathers (SOCIG) can be computed as (for the case of I_{v_p})

$$I_{v_p}(\mathbf{x}, \mathbf{h}) = \frac{2}{v_p^3} \left(\int \frac{\partial^2 (S_{+\mathbf{h}} p_h)}{\partial t^2} (S_{-\mathbf{h}} q_h) dt + \int \frac{\partial^2 (S_{+\mathbf{h}} p_v)}{\partial t^2} (S_{-\mathbf{h}} q_v) dt \right) , \tag{13}$$

where $S_{+\mathbf{h}}$ is a shifting operator that shifts the wavefield by $+\mathbf{h}$ in the $\mathbf{x}$ direction. Similarly, the operator $S_{-\mathbf{h}}$ shifts the wavefield in the opposite direction. Note that $(S_{+\mathbf{h}})^* = S_{-\mathbf{h}}$. $I_\epsilon(\mathbf{x}, \mathbf{h})$ and $I_\delta(\mathbf{x}, \mathbf{h})$ can be computed similarly. When the correct model is used for the construction of the seismic images, all the energy is focused at zero-lag ($\mathbf{h} = 0$). Moreover, the image extracted at $\mathbf{h} = 0$ corresponds to the one that can be obtained by stacking (along the angles dimension) the seismic image decomposed in angle gathers. The DSO objective function measures the nonfocused energy in the subsurface-offset-gathers and is thus minimized when performing WEMVA. On the other hand, the PSM measures the energy of the stack along the angles of the seismic image and has thus to be maximized.

I now show the computation of the gradients of the WEMVA inverse problem when the objective function is the DSO and using I_{v_p} as input. The same derivation can be used also to compute the gradients for the case of the PSM objective function. I follow a symbolic derivation based on the *adjoint-state* method (Plessix, 2006) that can be found in Li et al. (2012). For the sake of the notation, I indicate with $I_{\mathbf{h}}$ the generalized image $I_{v_p}(\mathbf{x}, \mathbf{h})$.

The first step is the definition of the Lagrangian augmented functional as

$$\begin{aligned}\mathcal{L}(\mathbf{p},\mathbf{q},I_{\mathbf{h}},\lambda,\mu,\gamma_{\mathbf{h}},\mathbf{m}) = &\sum_{\mathbf{h}}\frac{1}{2}\left\langle \mathbf{h}I_{\mathbf{h}},\mathbf{h}I_{\mathbf{h}}\right\rangle \\ &+\left\langle \lambda,\mathbf{f}-\mathbf{L}\mathbf{p}\right\rangle \\ &+\left\langle \mu,\mathbf{f}'-\mathbf{L}^{*}\mathbf{q}\right\rangle \\ &+\sum_{\mathbf{h}}\left\langle \gamma(\mathbf{x},\mathbf{h}),\frac{\partial\mathbf{L}^{*}}{\partial v_p}(S_{+\mathbf{h}}\mathbf{p})^{*}(S_{-\mathbf{h}}\mathbf{q})-I_{\mathbf{h}}\right\rangle .\end{aligned} \tag{14}$$

The adjoint-state equations can then be computed as

$$\begin{aligned}\frac{\partial\mathcal{L}}{\partial\mathbf{p}} &= -\mathbf{L}^{*}\lambda+\sum_{\mathbf{h}}\frac{\partial\mathbf{L}}{\partial v_p}(S_{+\mathbf{h}})^{*}(S_{-\mathbf{h}}\mathbf{q})\gamma_{\mathbf{h}}=0; \\ \frac{\partial\mathcal{L}}{\partial\mathbf{q}} &= -\mathbf{L}\mu+\sum_{\mathbf{h}}\frac{\partial\mathbf{L}}{\partial v_p}(S_{-\mathbf{h}})^{*}(S_{+\mathbf{h}}\mathbf{p})\gamma_{\mathbf{h}}=0; \\ \frac{\partial\mathcal{L}}{\partial I_{\mathbf{h}}} &= -\gamma_{\mathbf{h}}+\mathbf{h}^{2}I_{\mathbf{h}}=0.\end{aligned} \tag{15}$$

The solution of the adjoint-state equations allows the retrieval of the the adjoint-state variables $(\lambda(\mathbf{x},t),\mu(\mathbf{x},\mathbf{t}),\gamma(\mathbf{x},\mathbf{h}))$. The gradients of the objective function in equation 12 with respect to the three anisotropy parameters then can be computed as follows:

$$\begin{aligned}\nabla_{v_p}J_{\text{WEMVA}} &= \left\langle \lambda,-\frac{\partial\mathbf{L}}{\partial v_p}\mathbf{p}\right\rangle+\left\langle \mu,-\frac{\partial\mathbf{L}^{*}}{\partial v_p}\mathbf{q}\right\rangle ; \\ \nabla_{\epsilon}J_{\text{WEMVA}} &= \left\langle \lambda,-\frac{\partial\mathbf{L}}{\partial\epsilon}\mathbf{p}\right\rangle+\left\langle \mu,-\frac{\partial\mathbf{L}^{*}}{\partial\epsilon}\mathbf{q}\right\rangle ; \\ \nabla_{\delta}J_{\text{WEMVA}} &= \left\langle \lambda,-\frac{\partial\mathbf{L}}{\partial\delta}\mathbf{p}\right\rangle+\left\langle \mu,-\frac{\partial\mathbf{L}^{*}}{\partial\delta}\mathbf{q}\right\rangle .\end{aligned} \tag{16}$$

Generalized images

As previously discussed, I consider herein the model for the subsurface to be characterized by the three Thomsen parameters v_p,ϵ,δ. Equation 10 shows that in this case, the seismic images at our disposal are three as well. Regardless the choice of the specific cost function (either DSO or PSM), it is possible to minimize/maximize the objective function computed with any of the three images by computing the gradients with respect to the three parameters. In the derivation followed in the previous section, for instance, I derived the gradients of WEMVA for v_p, ϵ and δ by using I_{v_p}

as input. This input would correspond to find the anisotropic model, such that the image I_{v_p} has the desired characteristics. As a matter of fact, anisotropic WEMVA is often performed using only I_{v_p} and inverting for all the anisotropic parameters (Weibull and Arntsen (2014); Li et al. (2012)).

However, it is also possible to use the correspondent image when trying to invert for a specific parameter. This would mean, for instance, to minimize/maximize the DSO/PSM computed using I_{v_p} when inverting for v_p, I_ϵ for ϵ and I_δ for δ. The choice of the image to be used as input affects the computation of the WEMVA gradient. As a matter of fact, the seismic image chosen as input for WEMVA plays a role in the computation of the adjoint-state variables (equation 16). It is reasonable to expect the associated image to have a greater sensitivity to the correspondent image rather than the image computed for another parameter. All the parameters affect all the three images but each parameter produces a first-order effect to the correspondent image, and a second-order effect to the other two. If, for instance, I_{v_p} is used as input to invert for all the parameters, the inaccuracies in the ϵ and δ model would produce second-order effects on the image and they would thus be less significant than the effects caused by inaccuracies in the velocity model.

In the next section, I show the result of two preliminary tests I performed to validate the previous assumptions.

NUMERICAL TESTS

To validate my assumptions, I performed two tests. I computed the images I_{v_p} and I_ϵ using the correct v_p and δ models but varying the ϵ model. With the computed images, I evaluated the associated DSO and PSM objective functions values obtained with the different epsilon models.

Test 1

The velocity and epsilon models for the first test are shown in Figure 2. The first layer is isotropic with a vertical velocity of 2,000 meters per second (m/s). The second layer is characterized by a gradient (increasing with depth) in both the velocity and epsilon model starting at a depth of 800 meters (m). The initial values for the gradients in velocity and epsilon are, respectively, 2,000 m/s and 0. The final values (at $z = 1,800$ m) are 2,400 m/s for the velocity gradient and 0.3 for the parameter epsilon. A sharp contrast is inserted in the velocity model at a depth of 1,800 m while the epsilon model is constant below that depth. Using these models, I generated a synthetic dataset with a finite difference code based on the two-way wave-equation presented in the first section. The acquisition geometry is constituted of 61 sources that go from $x = 2,000$ m to $x = 14,000$ m at depth zero and receivers everywhere on the same surface as the sources. Receiver spacing is 20 m.

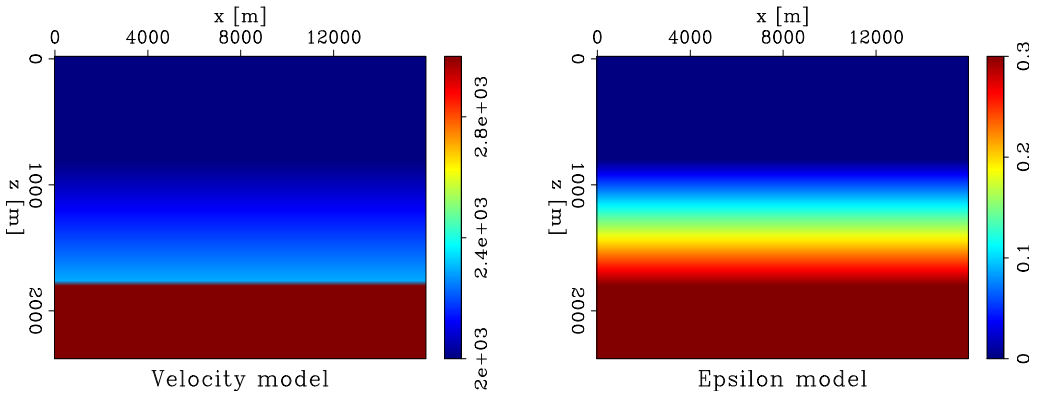

(a) (b)

Figure 2: Test 1. Vertical velocity (a) and epsilon (b) models used for the generation of the synthetic dataset. The initial values for the gradients in velocity and epsilon are, respectively, $2,000$ m/s and 0. The final values (at $z = 1,800$ m) are $2,400$ m/s for the velocity gradient and 0.3 for the parameter epsilon. [**ER**]

I generated different epsilon models by rescaling the gradient in the second layer: The initial value is always 0, while the final one (at $z = 1,800$ m) goes from 0.2 to 0.6. I used the different epsilon models to compute I_{v_p} and I_ϵ.

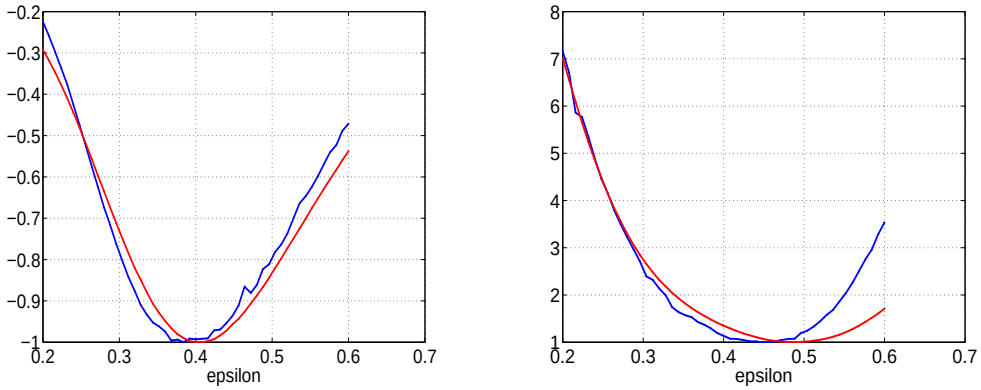

(a) (b)

Figure 3: Test 1. PSM (a) and DSO (b) curves computed using I_{v_p} (red) and I_ϵ (blue) with different epsilon models. The DSO curve associated to I_ϵ seems to indicate a greater sensitivity to the variations in the epsilon model. [**NR**]

The red curves in the graphs of Figure 3 show the values of the PSM (a) and DSO (b) objective function with respect to the epsilon model computed with I_{v_p}. The blue curves are the ones computed using I_ϵ. The curves obtained using the two different images are almost equivalent for the case of the PSM objective function. For the case of the DSO, though, the one associated to I_ϵ seems to indicate a greater sensitivity to the variations in the epsilon model. Indeed, especially around the minimum location, the DSO curve associated with I_ϵ is steeper than the one associated with I_{v_p}, meaning

that the same variation in the ϵ model produces a bigger change in I_ϵ rather than in I_{v_p}.

Test 2

The velocity and epsilon models for the second test are shown in Figure 4. The first layer is characterized by a constant vertical velocity of 2,000 m/s. The epsilon model is composed of a constant background ($\epsilon = 0$) with a Gaussian anomaly centered at $z = 1,200$ m and $x = 8,000$ m. The anomaly has a maximum value of 0.3. A sharp contrast that simulates a tilted reflector is inserted in both the velocity and epsilon models. The dip of the reflector is 5 degrees. These models were used to generate a synthetic dataset with the same acquisition geometry of Test 1.

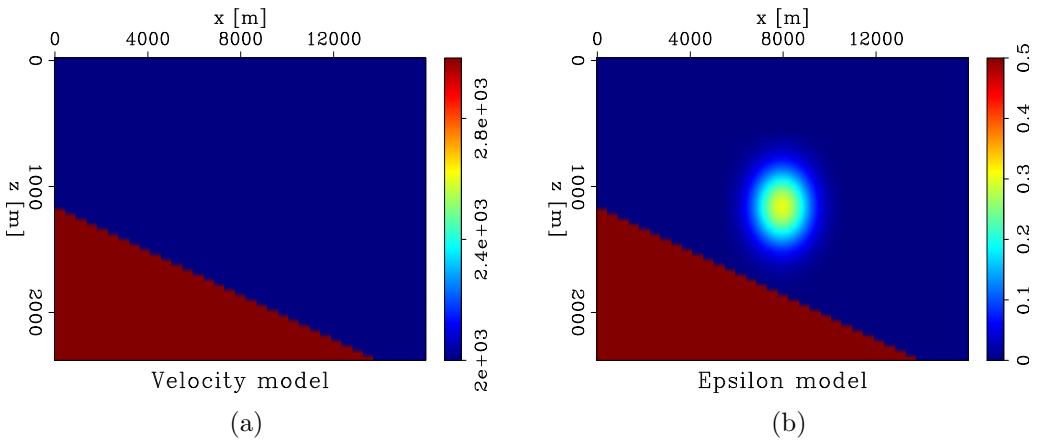

Figure 4: Test 2. Vertical velocity (a) and epsilon (b) models used for the generation of the synthetic dataset. [**ER**]

I generated the different epsilon models by rescaling the epsilon anomaly in the first layer. The shape of the anomaly is always the same, but the maximum value (at $x = 8,000$ m, $z = 1,200$ m) varies between 0 and 0.7. As for Test 1, I used the different epsilon models to compute I_{v_p} and I_ϵ.

The red curves in the graphs of Figure 5 show the values of the PSM (a) and DSO (b) objective function with respect to the epsilon model computed with I_{v_p}. The blue curves are the ones relative to I_ϵ. The curves computed with the two different images (I_{v_p} and I_ϵ) show more significant differences with respect to those of Test 1, probably because the fact that the dipping reflector enhance the contribution of the events associated with large reflection angles. These events are indeed the ones that carries most of the information about the parameter ϵ. Also in this case, the variations in the epsilon model seem to affect I_ϵ more than I_{v_p}.

The minimum/maximum of the curves in both tests do not coincide with the model

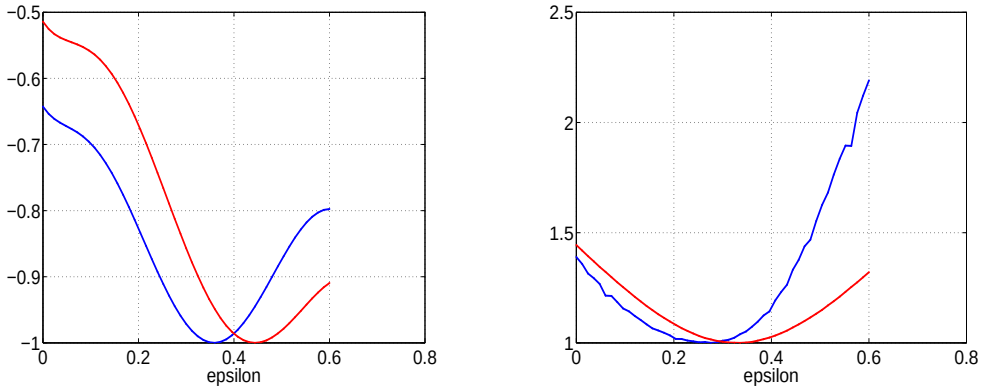

(a) (b)

Figure 5: Test 2. PSM (a) and DSO (b) curves computed using I_{v_p} (red) and I_ϵ (blue) with different epsilon models. Notice that the curves do not have their minimum at the same locations. The DSO curve associated to I_ϵ seems to indicate a greater sensitivity to the variations in the epsilon model. [**NR**]

used to generate the data (the minimum should be at $\epsilon = 0.3$). I attribute this to finite-difference acquisition artifacts. Moreover, the location of the minimum is different for the curves computed using I_{v_p} and I_ϵ and seems to be closer to the correct position when using the latter. More studies are needed to correctly analyze the problem.

CONCLUSIONS

In this paper, I presented a workflow for WEMVA derived using the VTI approximation. I used a pseudo-acoustic two-way wave-equation as the modeling engine. I also presented some preliminary results on the use of the generalized images as input for WEMVA. Although the preliminary tests seem to suggest that the proposed procedure could improve the accuracy and convergence rate of the velocity analysis, it is still unclear if the use of generalized images as input for WEMVA produces significant benefits with respect to the conventional approach.

FUTURE WORK

Additional work is needed to both evaluate the proposed WEMVA workflow based on the pseudo-acoustic two-way wave-equation and to further investigate the suggested approach of using the generalized images. For the first task, a code for the complete tomographic loop is needed. For the evaluation of the new proposed approach, on the other hand, further theoretical studies are needed for both gaining a better understanding of the problem and designing additional tests.

ACKNOWLEDGMENT

I would like to thank my advisor Giuseppe Drufuca, Nicola Bienati and Biondo Biondi for giving me the opportunity to spend some time working in the SEP group. I would like to thank Xukai Shen and Elita Li for helping me and letting me use their codes. Ali Almomin and Guillaume Barnier greatly helped me with useful ideas and suggestions. I would also thank all the people of the Stanford Exploration Project research group for their support and help.

REFERENCES

Alkhalifah, T., 1998, Acoustic approximations for processing in transversely isotropic media: Geophysics, **63**, 623–631.

Duveneck, E., P. Milcik, M. P. Bakker, and C. Perkins, 2008, Acoustic VTI wave equations and their application for anisotropic reverse-time migration: SEG Expanded Abstracts, **27**.

Fletcher, R., X. Du, and J. P. Fowler, 2009, Stabilizing acoustic reverse-time migration in TTI media: SEG Expanded Abstracts, **28**.

Grechka, V., L. Zhan, and J. W. Rector, 2004, Shear waves in acoustic anisotropic media: Geophysics, **69**, 576–582.

Li, Y. and B. Biondi, 2011, Migration velocity analysis for anisotropic models: SEG Expanded Abstracts.

Li, Y., P. Shen, and C. Perkins, 2012, Vti migration velocity analysis using RTM: SEP-Report, **147**, 57–72.

Plessix, E. R., 2006, A review of the adjoint-state method for computing the gradient of a funtional with geophysical applications: Geophys. J. Int., **167**, 495–503.

Sava, P. and S. Fomel, 2006, Generalized imaging conditions for wave equation migration: CWP report, 524.

Shen, P., 2004, Wave equation migration velocity analysis by differential semblance optimization: PhD thesis, Rice University.

Symes, W. W. and M. Kern, 1994, Inversion of reflection seismograms by differential semblance analysis: Algorithm structure and synthetic examples: Geophysics, **42**, 565–614.

Tarantola, A., 1984, Inversion of seismic reflection data in the acoustic approximation: Geophysics, **49**, 1259–1266.

Thomsen, A. L., 1986, Weak elastic anisotropy: Geophysics, **51**, 1954–1966.

Toldi, L. J., 1989, Velocity analysis without picking: Geophysics, **54**, 191–199.

Weibull, W. W. and B. Arntsen, 2014, Anisotropic migration velocity analysis using reverse-time migration: Geophysics, **79**.

Zhang, Y. and H. Zhang, 2009, A stable TTI reverse time migration and its implementation: SEG Expanded Abstracts, **28**, 3–11.